Chapter Three

Easy-Plane Ferromagnet Kink-Antikink Scattering

3.1 Numerical Method and Results

A kink-antikink ($K\bar{K}$) pair collision can be initiated by starting with a sG kink-antikink pair, and following the time evolution of the discrete equations of motion (2-5) for specified α and β (Wysin et al. 1984). The initial condition is then given by

$$\phi(\xi,\tau) = 4 \tan^{-1} \frac{\sinh[\gamma b^{1/2} u_{sG}(\tau-\tau_0)]}{u_{sG}\cosh(\gamma b^{1/2}\xi)} \qquad (3\text{-}1a)$$

$$\theta(\xi,\tau) = \phi_\tau \quad . \qquad (3\text{-}1b)$$

If this profile were to evolve exactly according to sine-Gordon dynamics, then $2u_{sG}\tau_0$ would be the initial spatial separation of the kink and antikink, each moving with speed u_{sG} toward the other. The parameter τ_0 would be the time before the collision. But since a kink moves more slowly ($u < u_{sG}$), the actual time interval before the collision is longer.

Again periodic boundary conditions on systems up to 180 spins were used; we used the same integration scheme as for the single kink simulations. The final state of the system was observed up to a time roughly ten times τ_0. The system profile was also observed at intermediate times. A variety of final states was found possible. In Figure 3.1, we show a final state phase diagram in the u_{sG}-b plane. Again, we fixed $\alpha = 2A/J = 0.0954$, and varied β. The initial velocity u_{sG} can be interpreted as the system's initial energy, which unfortunately will also include some spin wave energy. Later we describe a method where this problem can be avoided, by using time averaged profiles for the initial conditions, together with Neumann boundary conditions.

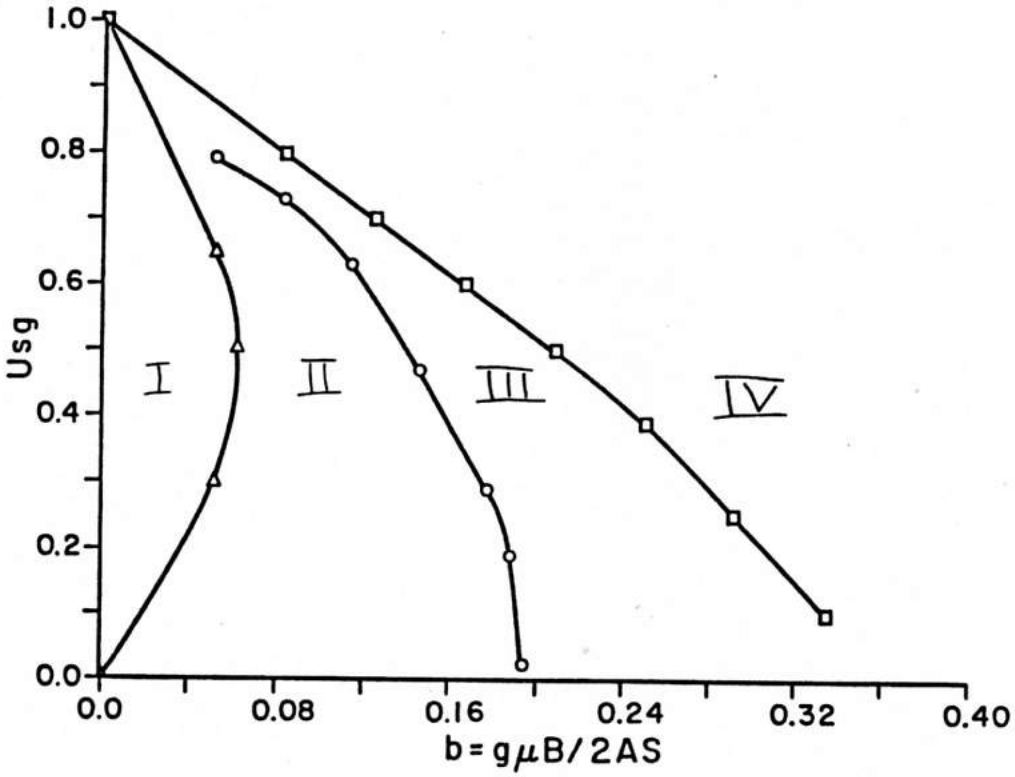

Figure 3.1 Final state phase diagram for $K\bar{K}$ scattering, as a function of the velocity u_{sG} of the input sG pair, and the magnetic field $b = g\mu_B B/2AS$. In region I, the pair undergo sG transmission. In region II, an oscillating breather-like state is formed. In region III, they are reflected, with a change in speed due to transfer between branches II and III. In region IV, they are reflected, with no change in speed, since the transition is from branch III to branch III. Along the line separating regions III and IV the kinks are the second static kinks. (The maximum energy kinks for a given field).

There are four major regions to the phase diagram. Generally, at low fields b, the pair undergo transmission (region I). At slightly higher fields, they form a bound state, that is, a breather mode (region II). At higher fields, the pair reflect from each other, and can transfer from branch II to branch III (region III). Finally, at still higher fields, this reflection also occurs, but involves branch III to branch III bouncing (region IV). This is necessarily the case for $b > \frac{1}{3}$, where only branch III exists.

In Figure 3.2, ϕ and θ profiles at various times during a collision in region I, where $b < b_1(u_{sG})$, are shown. The solitons pass through each other with little change in profile or velocity, consistent with a slightly perturbed sG interpretation. This occurs only up to $b \lesssim 0.06$, considerably less than the critical field. Also, even for $u_{sG} \to 0$, $b_1 \to 0$. Thus the sG description for collisions is not valid even at low velocities. Instead, low velocity collisions can lead to breathers for small fields $b \lesssim 0.19$. This is a possibly a balance of the collison time versus energy dissipation. We know from the linear stability analysis that a single kink has a bound state mode which goes "unstable" at $b_c = \frac{1}{3}$ for $u = 0$, in addition to the zero frequency translation mode. For $b < b_c$, this bound state mode corresponds to localized internal oscillations which can remove energy from the translational energy of the kink during a collision. At small kink velocities, the duration of the collision is such that these oscillatory modes have adequate time to be excited, and the $K\bar{K}$ pair form a breather. Near $u_{sG} \lesssim 0.5$, where $b_1(u_{sG}) \lesssim 0.06$, the maximum, the <u>actual</u> kink velocity u is maximum; therefore, at this point the collision has the shortest duration, and is most likely to result in transmission. For $u_{sG} > 0.5$, the actual velocity

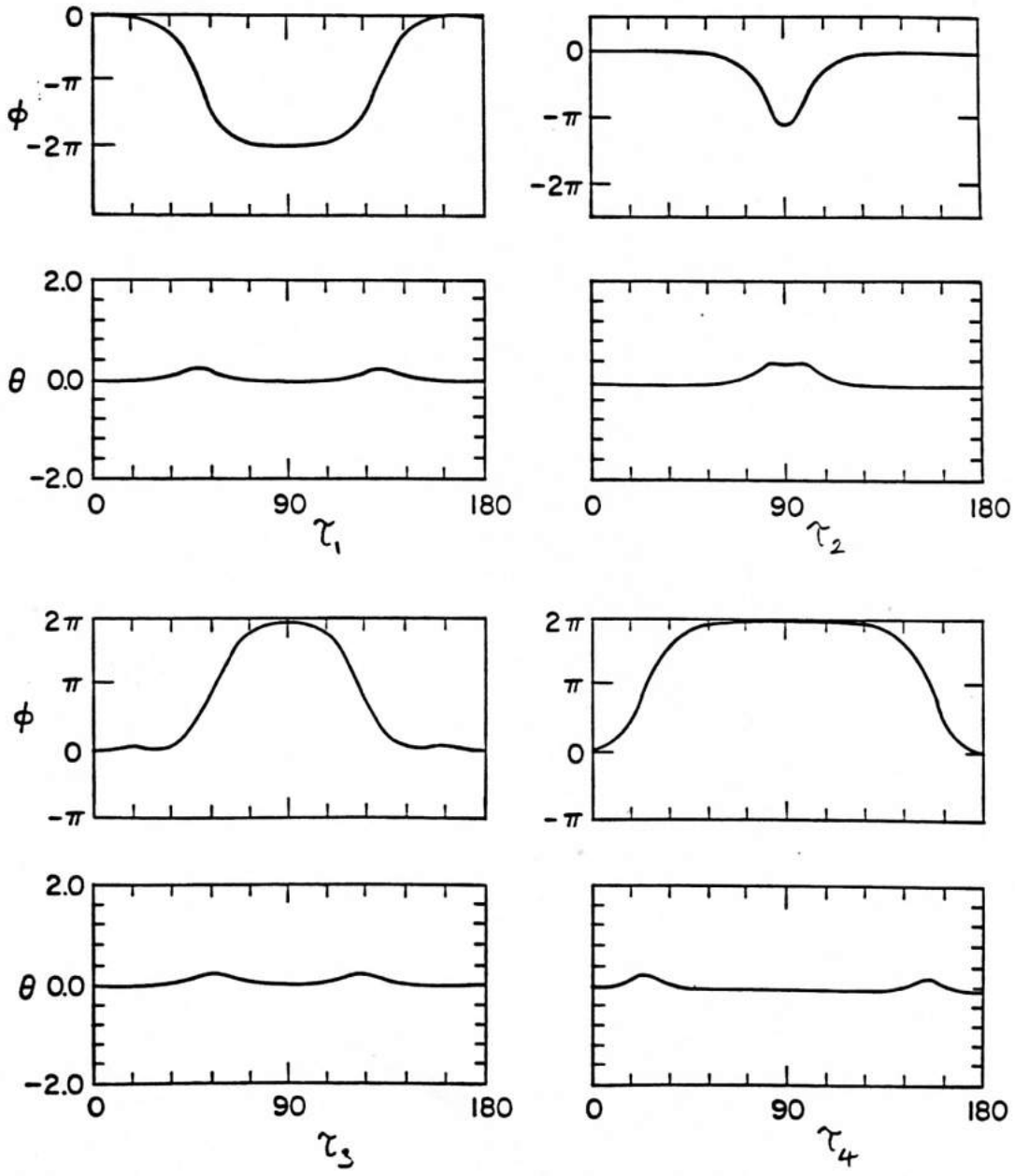

Figure 3.2 Details of a region I collision at a sequence of times τ_1, τ_2, τ_3, τ_4, for b = 0.025, u_{sG} = 0.60. ϕ and θ are the in-plane and out-of-plane angles respectively.

begins to decrease, and therefore the collision duration increases, and breather formation is more likely. This argument explains the qualitative shape of $b_1(u_{sG})$.

In Figure 3.3, details of a collision in region II ($b_1(u_{sG}) < b < b_2(u_{sG})$) are shown. The pair collides and forms a "breather" bound state, or some general oscillatory structure. An interesting feature of this region is the presence of a transmission "window" for $u_{sG} = 0.4$ and $0.1258 < b < 0.1289$. In Figure 3.4, the breather period is shown for $u_{sG} = 0.4$, as a function of b. As $b \to b_1$, the breather period diverges as expected when entering the sG transmission regime. Within the window, the pair undergo transmission. For $0.14 < b < b_2 (\simeq 0.16)$, the pair appear to decay to oscillations, before entering region III.

In region III ($b_2(u_{sG}) < b < b_3(u_{sG})$), the pair is reflected during the collision. Collision details are shown in Figure 3.5. A low velocity branch I or branch II kink (a "forward" kink) emerges from the collision as a faster moving branch III kink (a "backward" kink). This is understood through use of the single kink symmetrized dispersion curve, shown in Figure 3.6 for $b < b_c$. On branch I or II, we have $\theta_m > 0$ for $u > 0$, where θ_m is the maximum out-of-plane angle at the center of the kinks, or the Liebmann Ansatz parameter. On branch III, however, $\theta_m > 0$ for $u < 0$ (by definition). During a collision involving a branch I or branch II kink starting with $u > 0$, the velocity u passes through zero while θ_m increases smoothly, resulting in an equal energy branch III kink with $u < 0$ and θ_m larger than its initial value. Similarly, the reverse process should be allowed, and in fact branch III to branch II transfer has been observed. With the periodic boundary conditions, we have obtained a sequence of collisions where a kink alternates between branch II and branch III after each collision, for $b = 0.21$ and $u_{sG} = 0.3$ (see Figure 3.13).

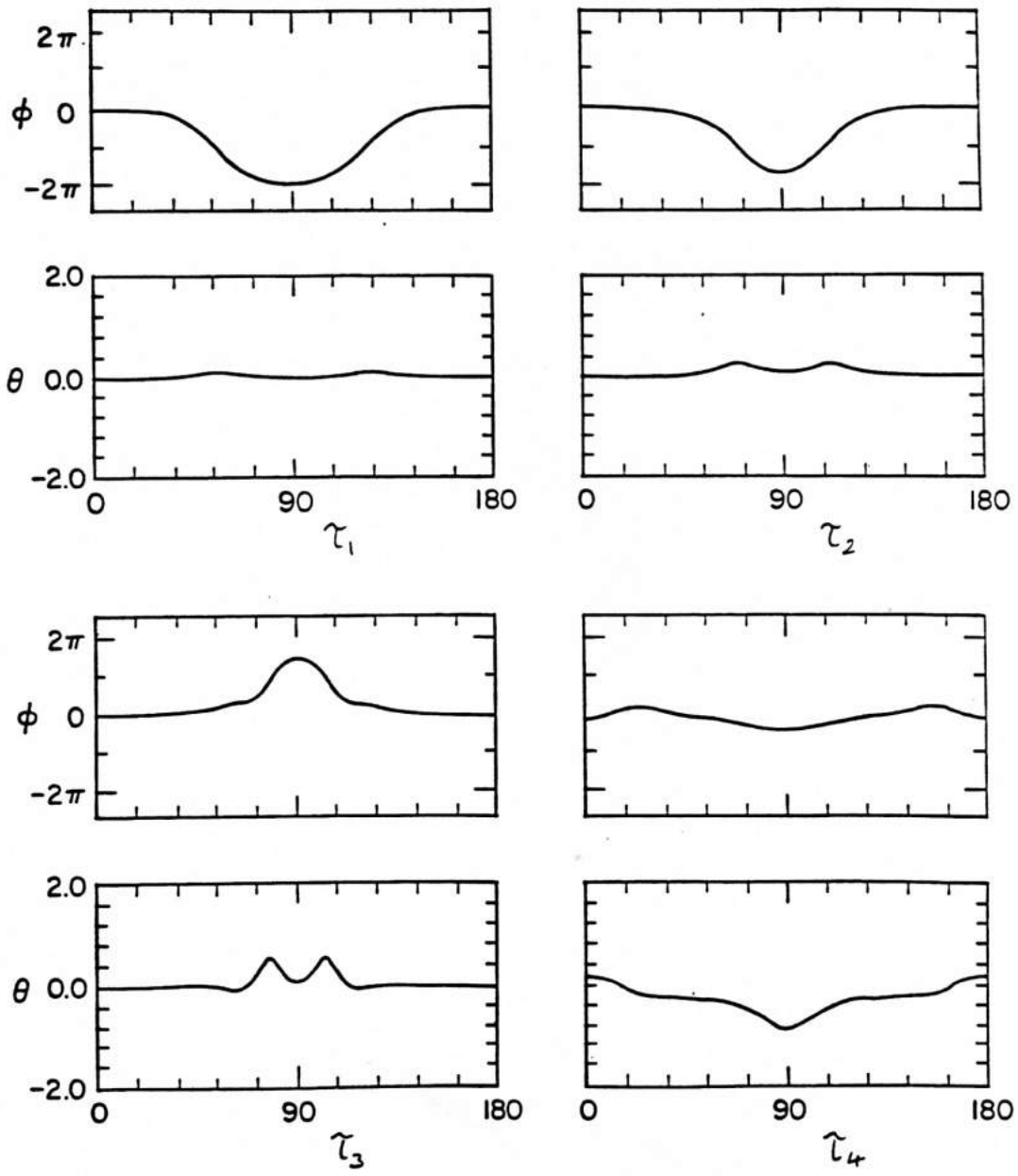

Figure 3.3 Details of a region II collision at a sequence of times τ_1, τ_2, τ_3, τ_4, for b = 0.084, u_{sG} = 0.10.

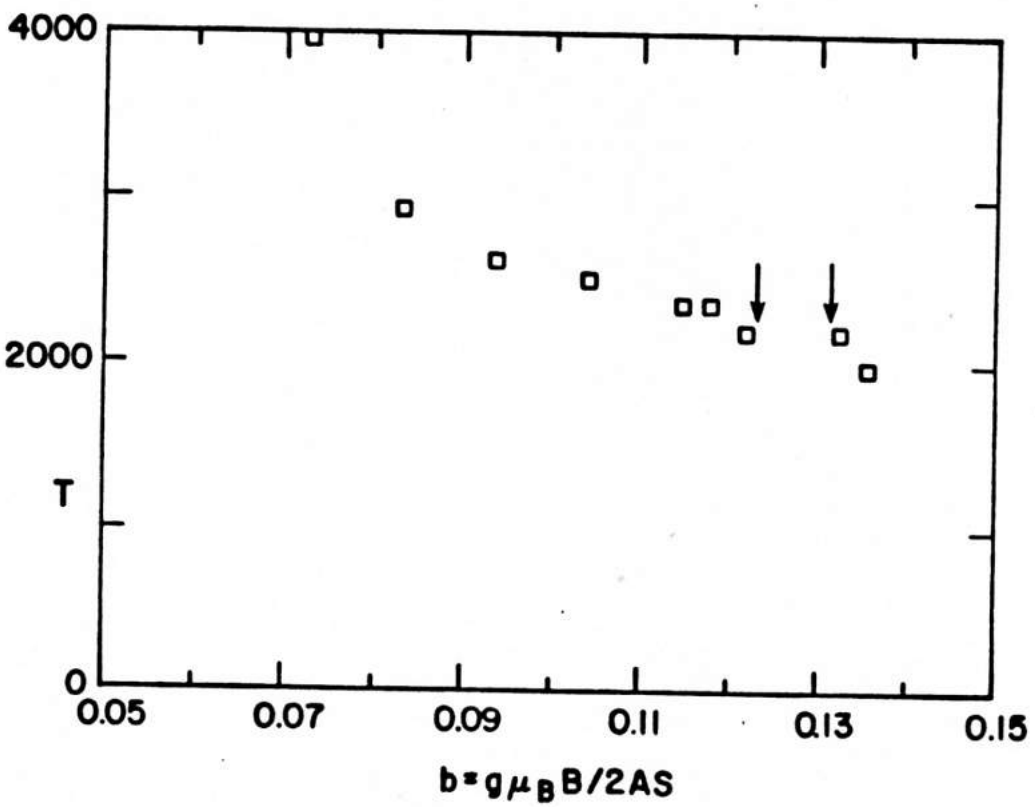

Figure 3.4 Breather period, T, in region II as a function of magnetic field b for $u_{sG} = 0.4$. The boundary between regions I and II is characterized by a divergence in T. However, no such divergence takes place at the boundary between regions II and III. Instead, preceding time boundary is a transmission window, indicated by arrows.

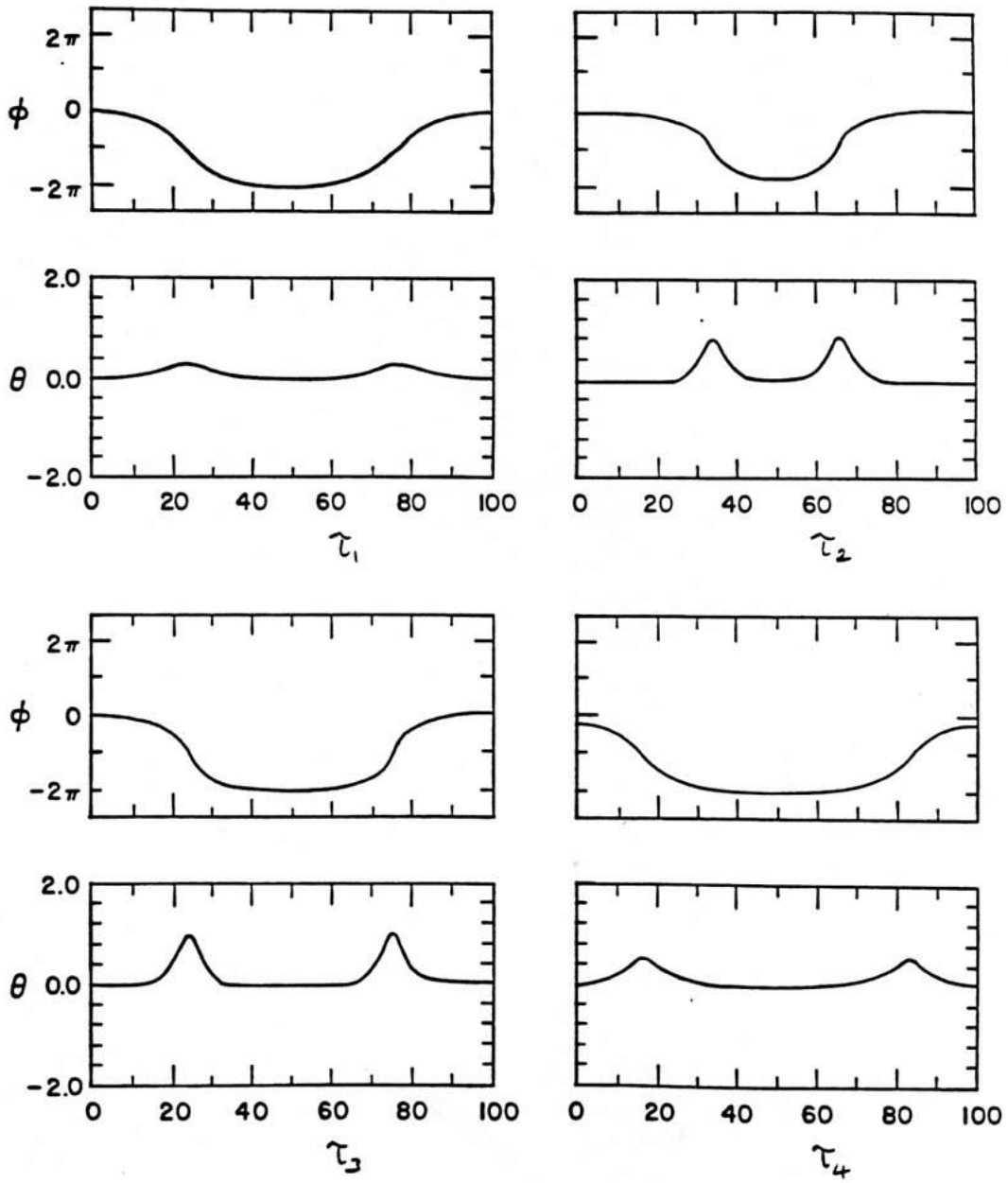

Figure 3.5 Details of a region III collision of a sequence of time τ_1, τ_2, τ_3, τ_4, for b = 0.21, u_{sG} = 0.30.

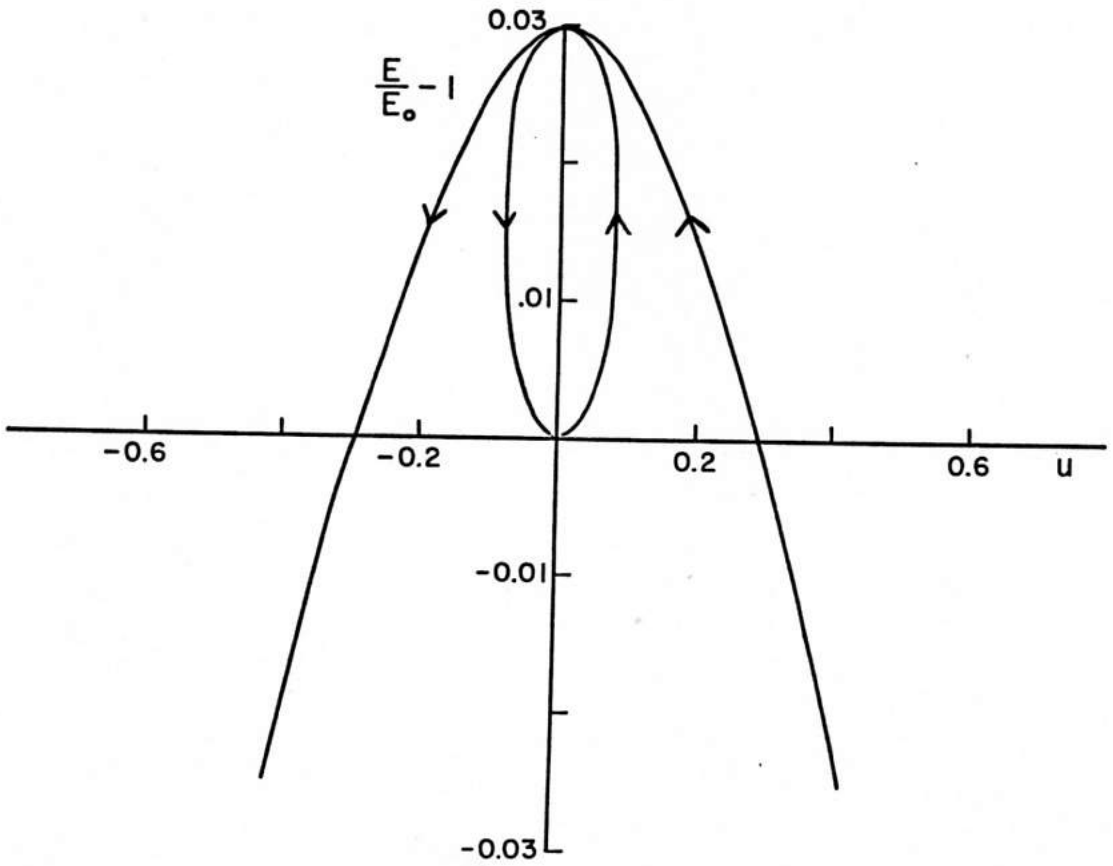

Figure 3.6 The numerically determined symmetrized kink dispersion for b = 0.2096, less than the critical field. The arrows indicate the direction of increasing θ_m, the Liebmann Ansatz parameter. At the origin $\theta_m = 0$, and the range of θ_m can be from $-\pi$ to π.

Branch II to branch II transitions have not been observed, and seem to be forbidden. They would require θ_m to be increasing ($\dot{\theta}_m > 0$, moving in the direction of the arrows in Figure 3.6) and change sign while starting from a positive value, which is impossible without a discontinuity in θ_m.

In region IV ($b > b_3(u_{sG})$), the incoming kinks are on branch III. Along the curve $b_c(u_{sG})$, the kinks are the static distorted kinks previously discussed in Chapter 2, so that everything to the right is on branch III. During a collision here, the pair is reflected and emerges on the same branch, but with reversed velocity. Details are shown in Figure 3.7. Refering to the single kink symmetrized dispersion relation, for $b < b_c$ (Figure 3.6) or $b > b_c$ (Figure 3.8), it is easy to see that this should be allowed. Starting from a branch III kink with $u > 0$ and $\theta_m < 0$, u decreases during the collision while θ_m increases towards zero. The velocity u passes through zero to a negative value, while θ_m continues to increase to a positive value, without any discontinuity. The kink emerges with no loss of energy, but with u and θ_m reversed in sign. Note that for $b > \frac{1}{3}$ only branch III exists. These collisions have been observed up to $b \lesssim 0.5$, for small u_{sG}. At larger u_{sG}, excess spin wave generation makes interpretation of the collision results difficult.

A preferable way to perform the above collision experiments is to use a time-averaged single kink as the initial condition, to remove spin waves from the system. Then using this profile to initiate a simulation with Neumann boundary conditions (zero derivative at the boundaries) is equivalent to the kink scattering from its mirror image (i.e. an antikink) at the boundaries. A further advantage of this method is that the number of lattice sites necessary is reduced by a factor of 2. If we were to do this experiment systematically, the u_{sG}-b phase diagram would be replaced

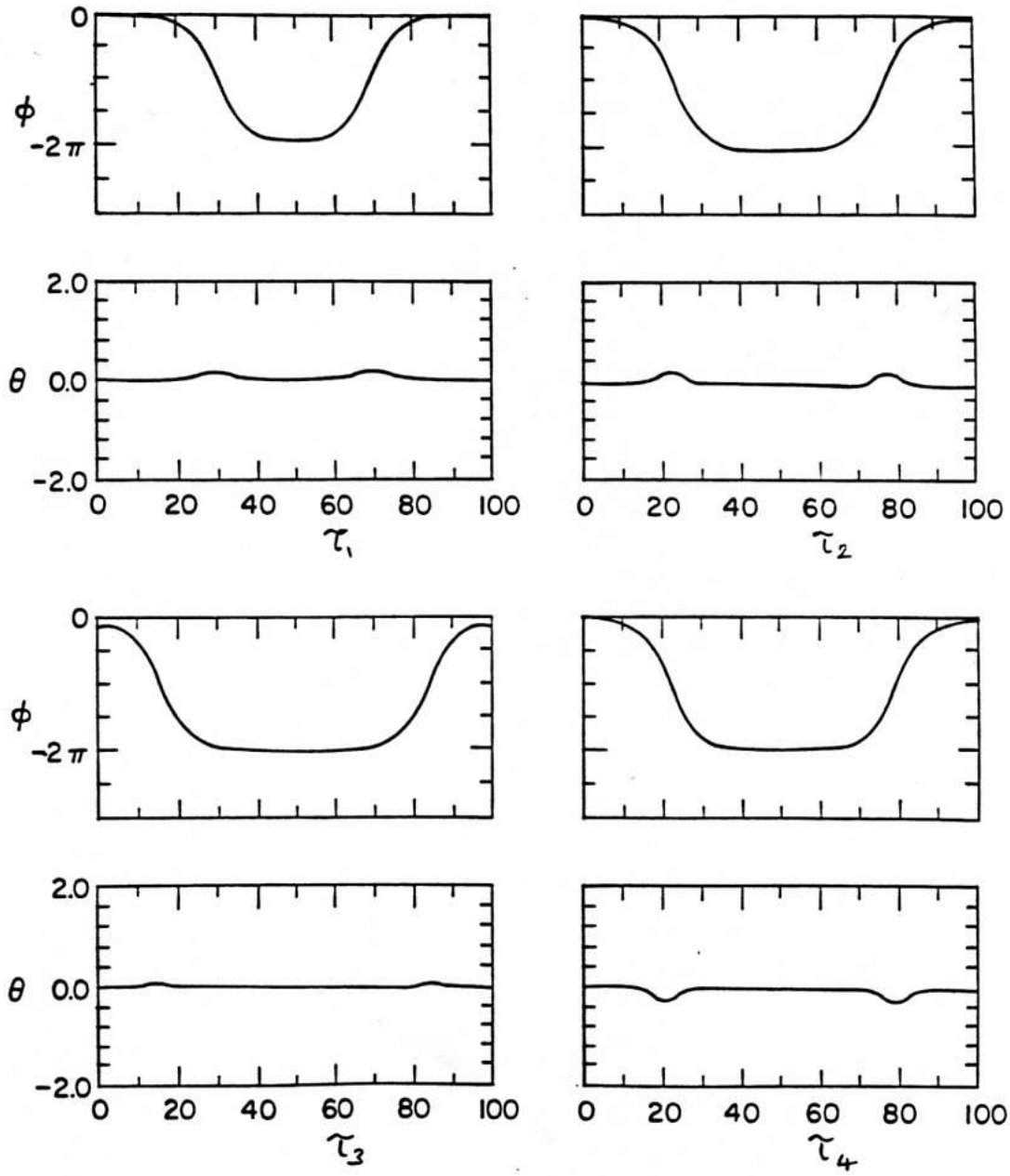

Figure 3.7 Details of a region IV collision at a sequence of times τ_1, τ_2, τ_3, τ_4, for b = 0.47, u_{sG} = 0.10.

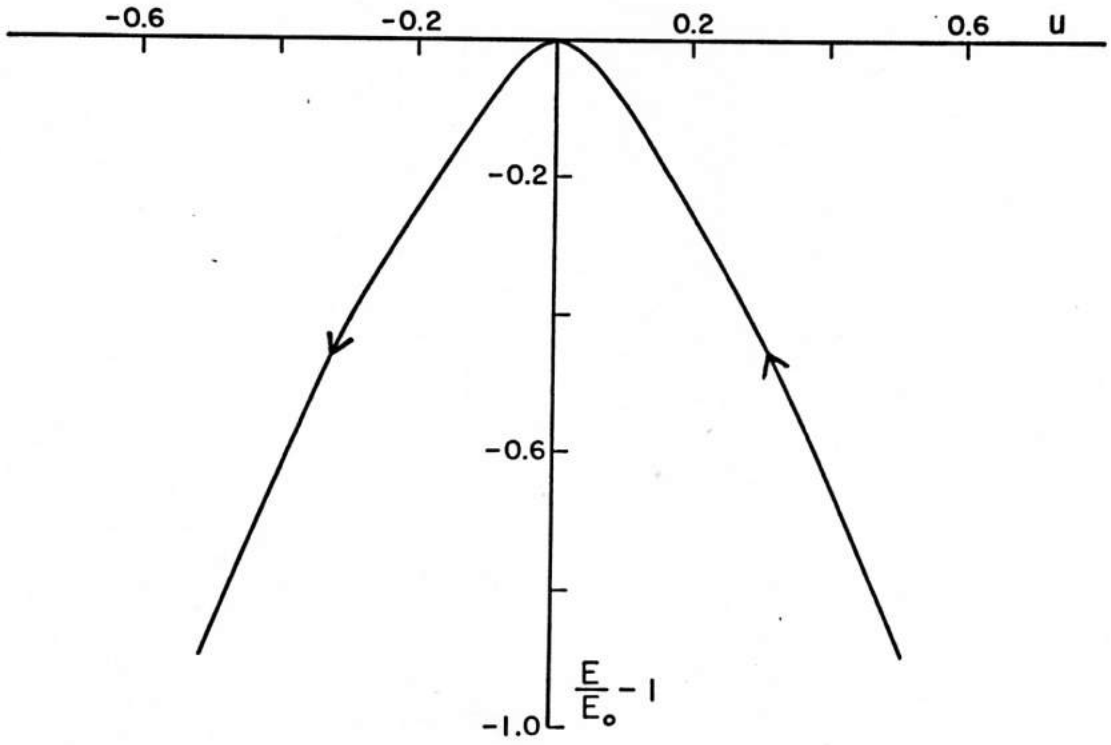

Figure 3.8 A typical symmetrized dispersion curve for $b > b_c$. The arrows indicate the direction of increasing θ_m, the Liebmann Ansatz parameter. At the origin $\theta_m = 0$, and the range of θ_m can be from $-\pi$ to π.

by a more appropriate θ_m-b phase diagram for the final states. The parameter u_{sG} partly loses its meaning after the time averaging, and the average velocity $\bar{u}$ is not a good parameter either since a single value of $\bar{u}$ can correspond to two different energy kinks. Similarly the energy cannot be used; the only parameter which uniquely specifies all the kink properties is θ_m, and so it should be used in the phase diagram.

A complete θ_m-b phase diagram has not been constructed. We have tested these ideas by starting with a sG kink of velocity u_{sG}, performing the time averaging to produce a kink of velocity u, and observing that the resulting collision was consistent with the results of the u_{sG}-b phase diagram. Figures 3.9-3.16 show space-time plots of collisions in regions I, II, III and IV of the u_{sG}-b phase diagram, as obtained by this method.[1] Certainly $0 < u_{sG} < 1$ will map approximately onto $0 < \theta_m < \pi$, and so in some sense u_{sG} is equivalent to θ_m, excluding the unknown effects of the spin waves during the collision. But we believe that the simulations done here give the general features of $K\bar{K}$ scattering, especially in the low u_{sG} regime where spin wave generation is negligible. Probably only some minor details will be changed by using the more appropriate θ_m-b phase diagram.

3.2 Discussion: Is sine-Gordon Adequate for Easy-Plane Ferromagnets?

The above numerical results show the inadequacy of a sG description of $K\bar{K}$ scattering. Only for a limited region of parameter space is the sG description valid. Generally, $K\bar{K}$ scattering can lead to transmission for small b, breather and oscillatory status for slightly larger b, and $K\bar{K}$ reflection at larger values of b, both above and below b_c. The internal

---

[1] A system of $\frac{1}{2}N$ spins with Neumann boundary conditions and one kink was simulated, and plots of N spins were produced by reflection about one boundary. The resulting plots represent $K\bar{K}$ collisions on a system with periodic boundary conditions.

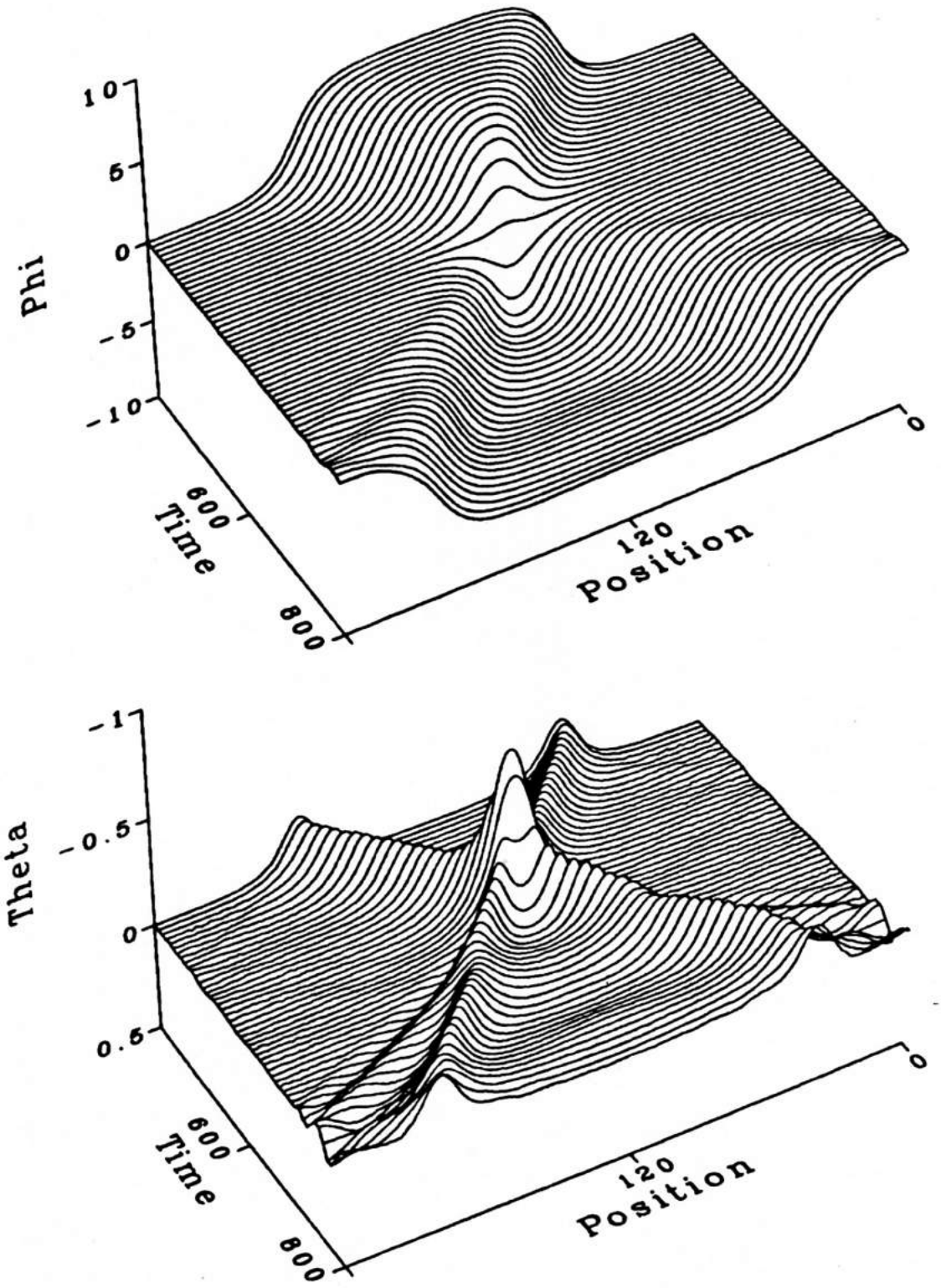

Figure 3.9 Space-time $K\bar{K}$ profile obtained by using a time-averaged initial profile with b = 0.025, u_{sG} = 0.60, resulting in a region I collision. The pair transmit with a small production of spin wave modes.

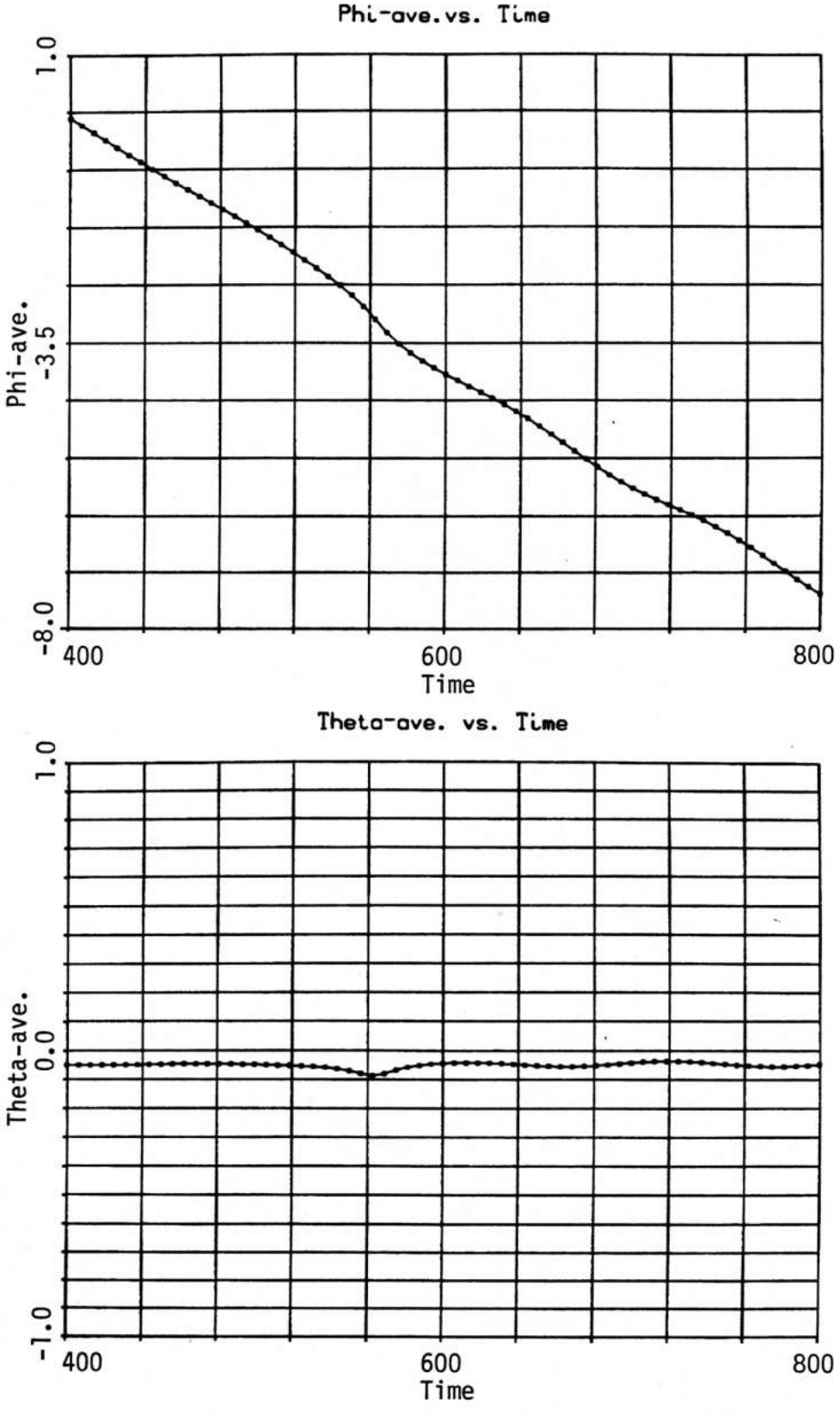

Figure 3.10a Spatial averages of ϕ and θ vs. time for the region I collision of Figure 3.9.

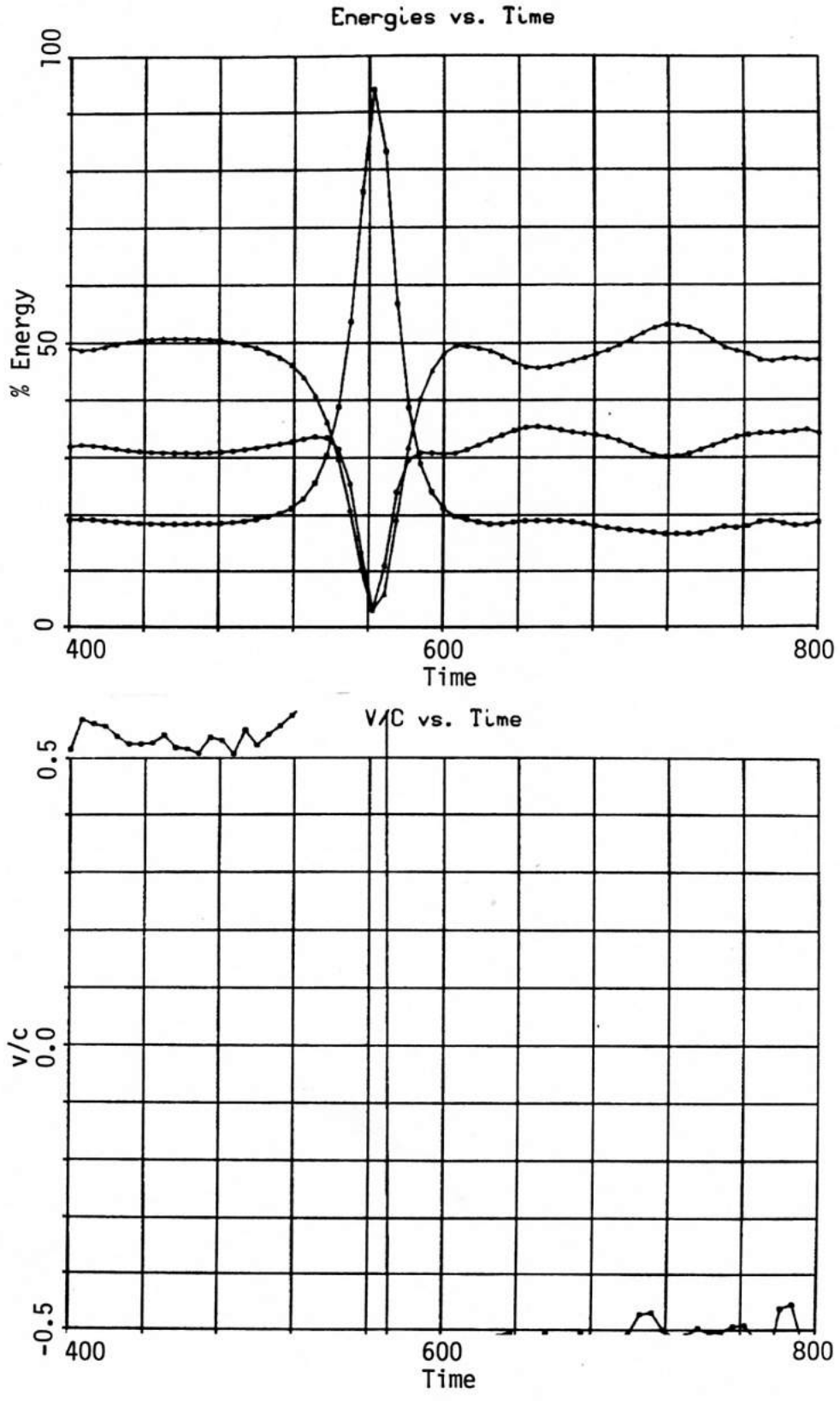

Figure 3.10b Anisotropy (□), field (0), exchange (Δ) energies and velocity vs. time for the region I collision of Figure 3.9.

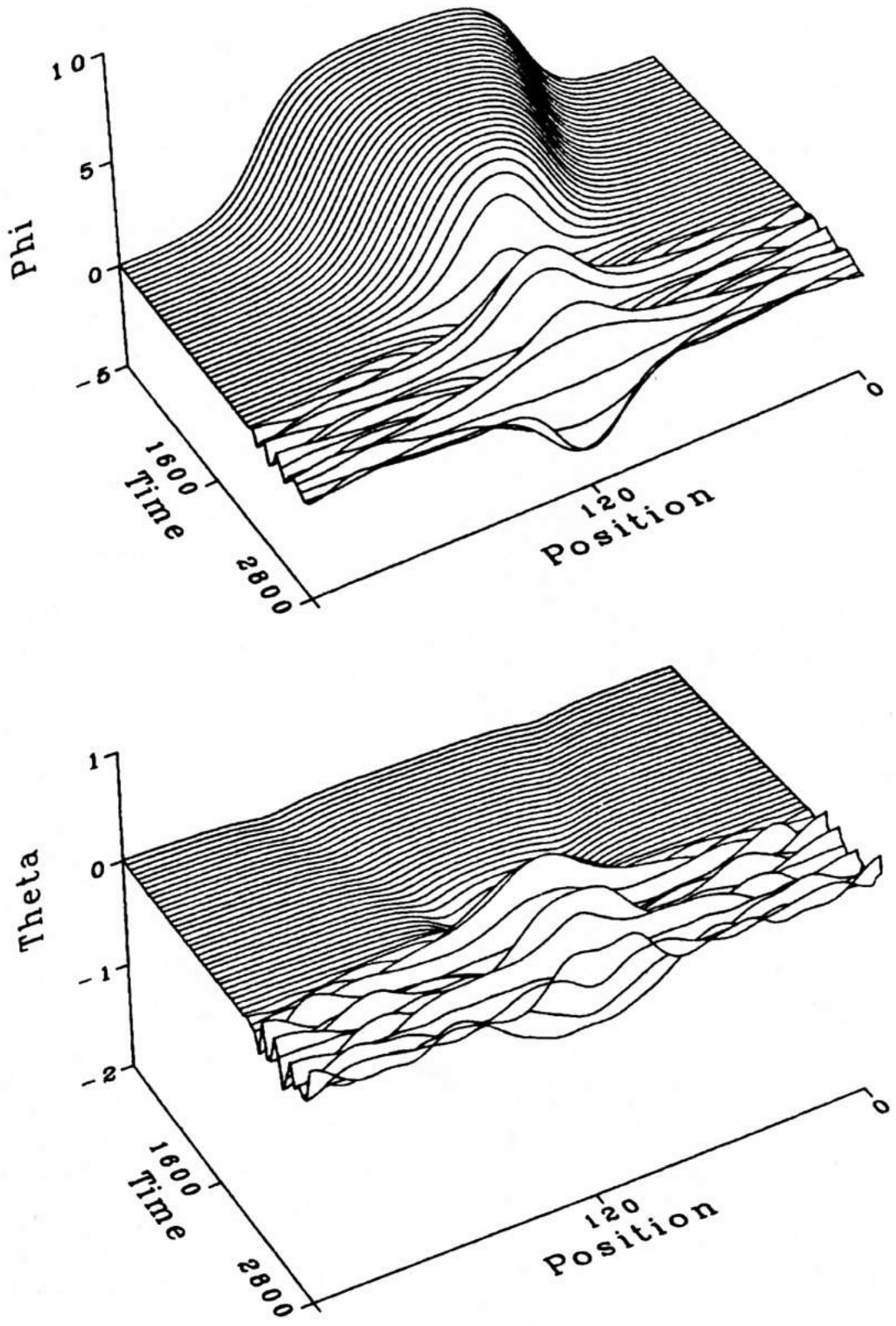

Figure 3.11 Space-time $K\bar{K}$ profile obtained by using a time-averaged initial profile with b = 0.084, u_{sG} = 0.10, resulting in a region II collision. The pair form a bound oscillatory breather-like mode.

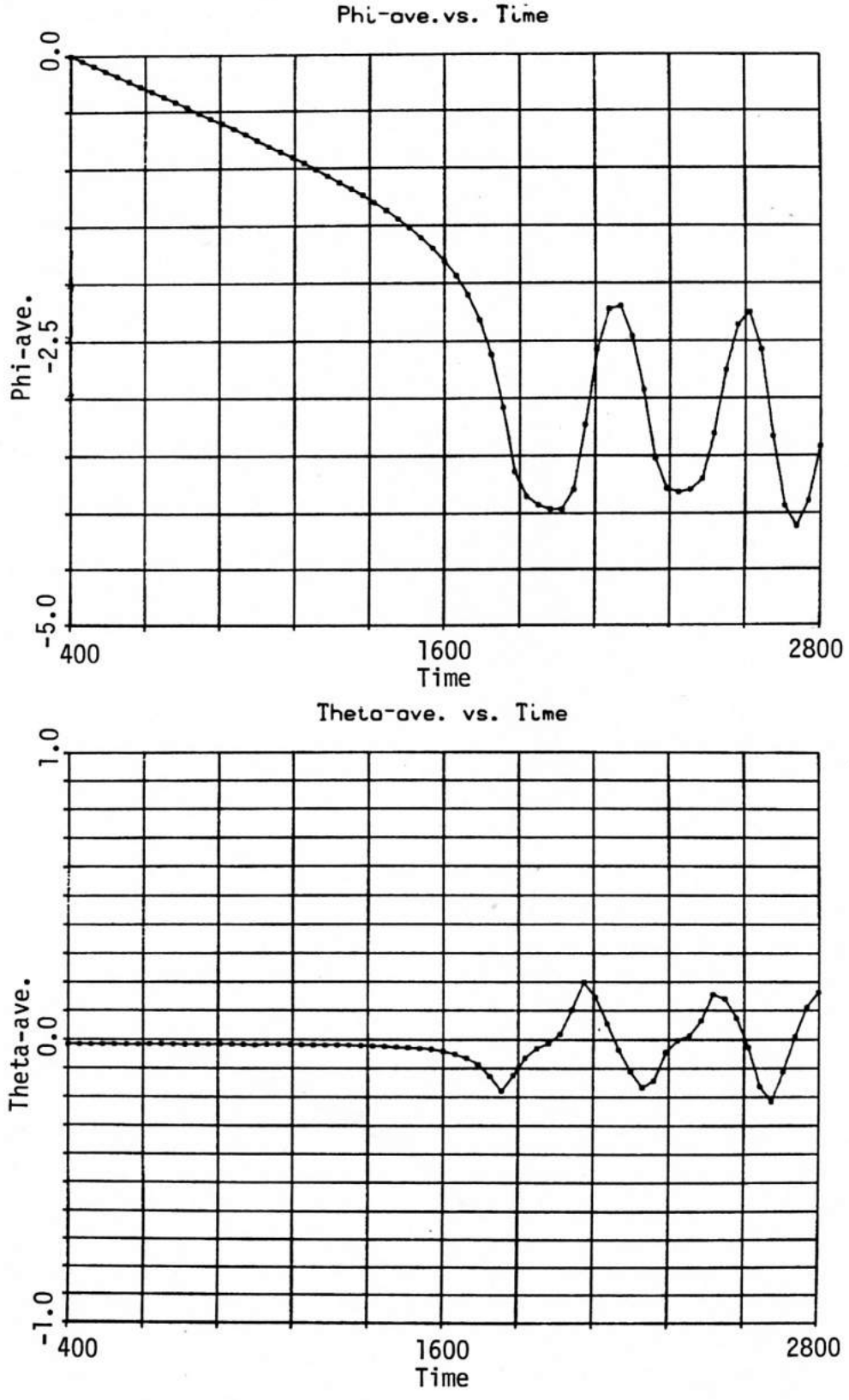

Figure 3.12a Spatial averages of ϕ and θ vs. time for the region II collision of Figure 3.11.

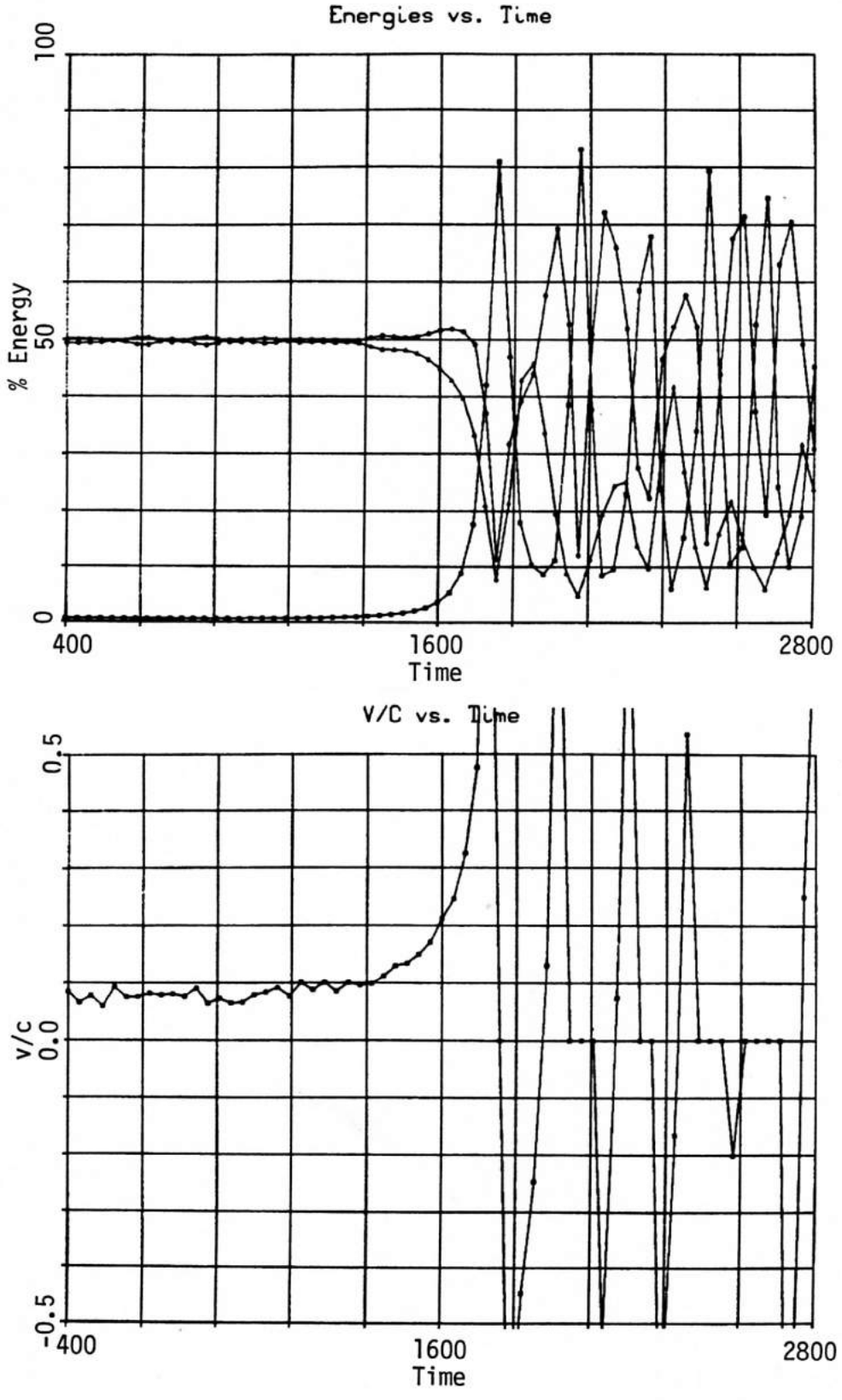

Figure 3.12b Anisotropy (□), field (0), exchange (Δ) energies and velocity vs. time for the region II collision of Figure 3.11.

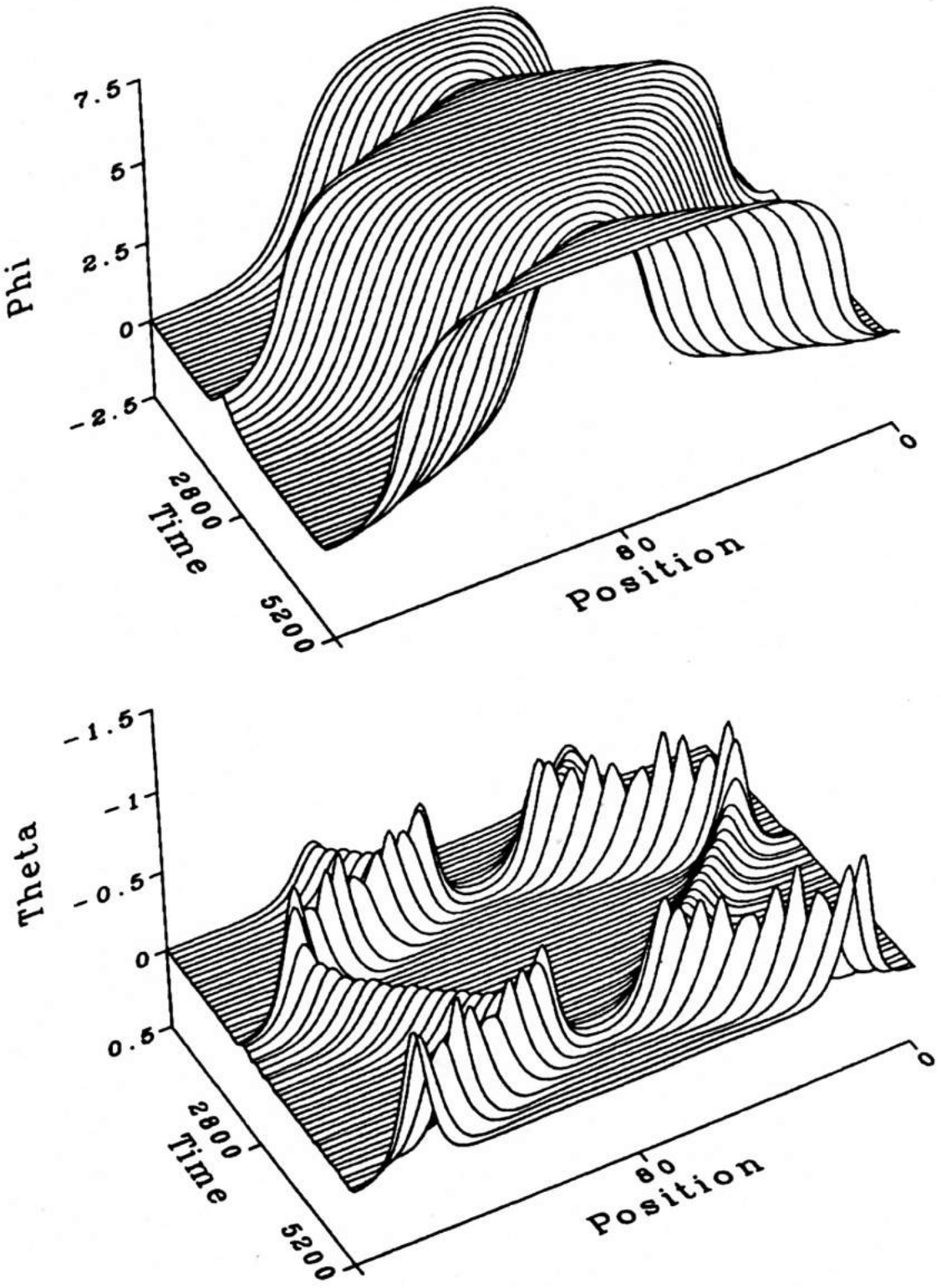

Figure 3.13 Space-time $K\bar{K}$ profile obtained by using a time-averaged initial profile with b = 0.2096, u_{sG} = 0.30, resulting in a region III collision. The pair reflects, converting to faster b ranch III kinks. Upon interacting again at the boundaries, the transition is back to the initial branch II kinks. Then the initial collision repeats.

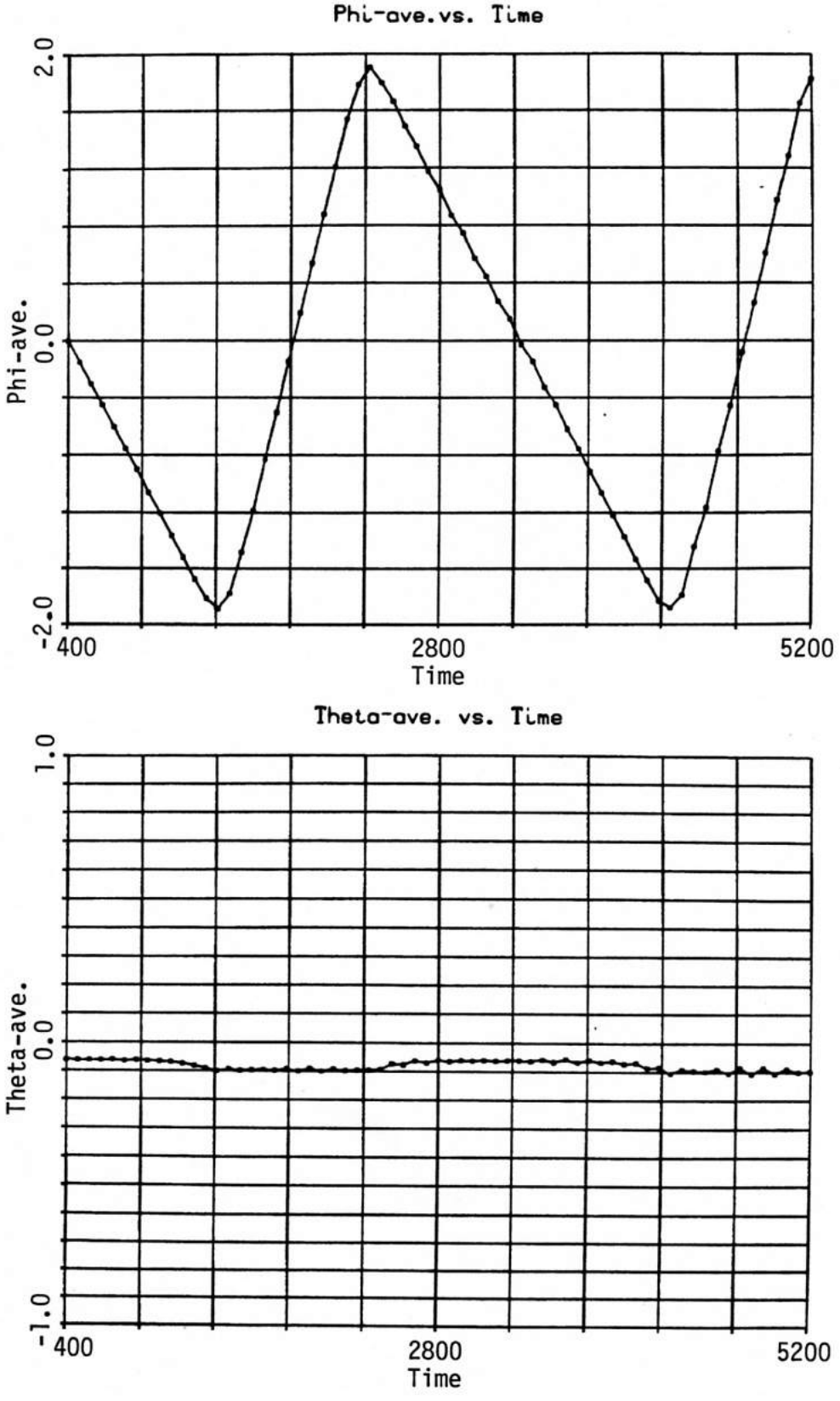

Figure 3.14a Spatial averages of ϕ and θ vs. time for the region III collision of Figure 3.13.

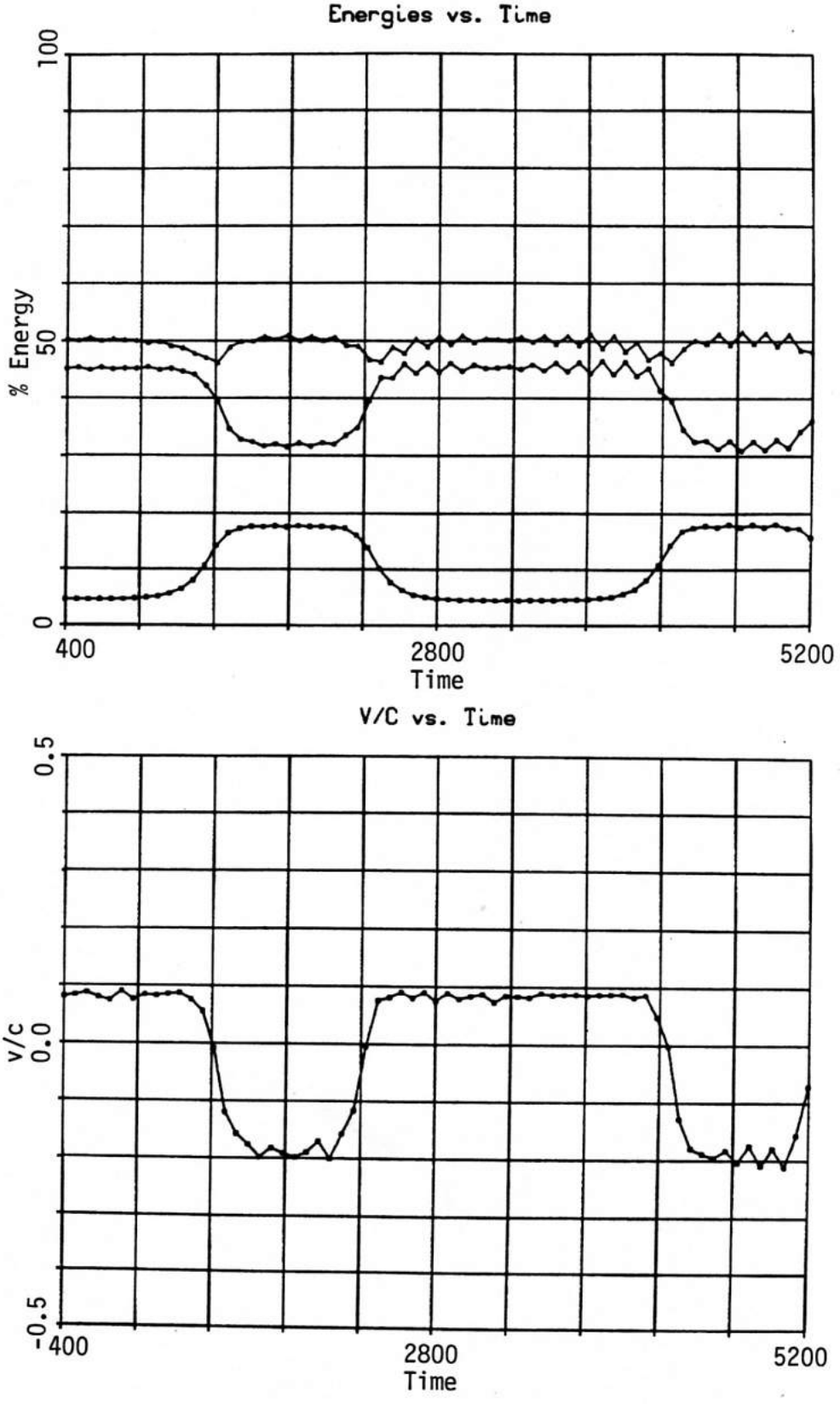

Figure 3.14b Anisotropy (□), field (0), exchange (Δ) energies and velocity vs. time for the region III collision of Figure 3.13.

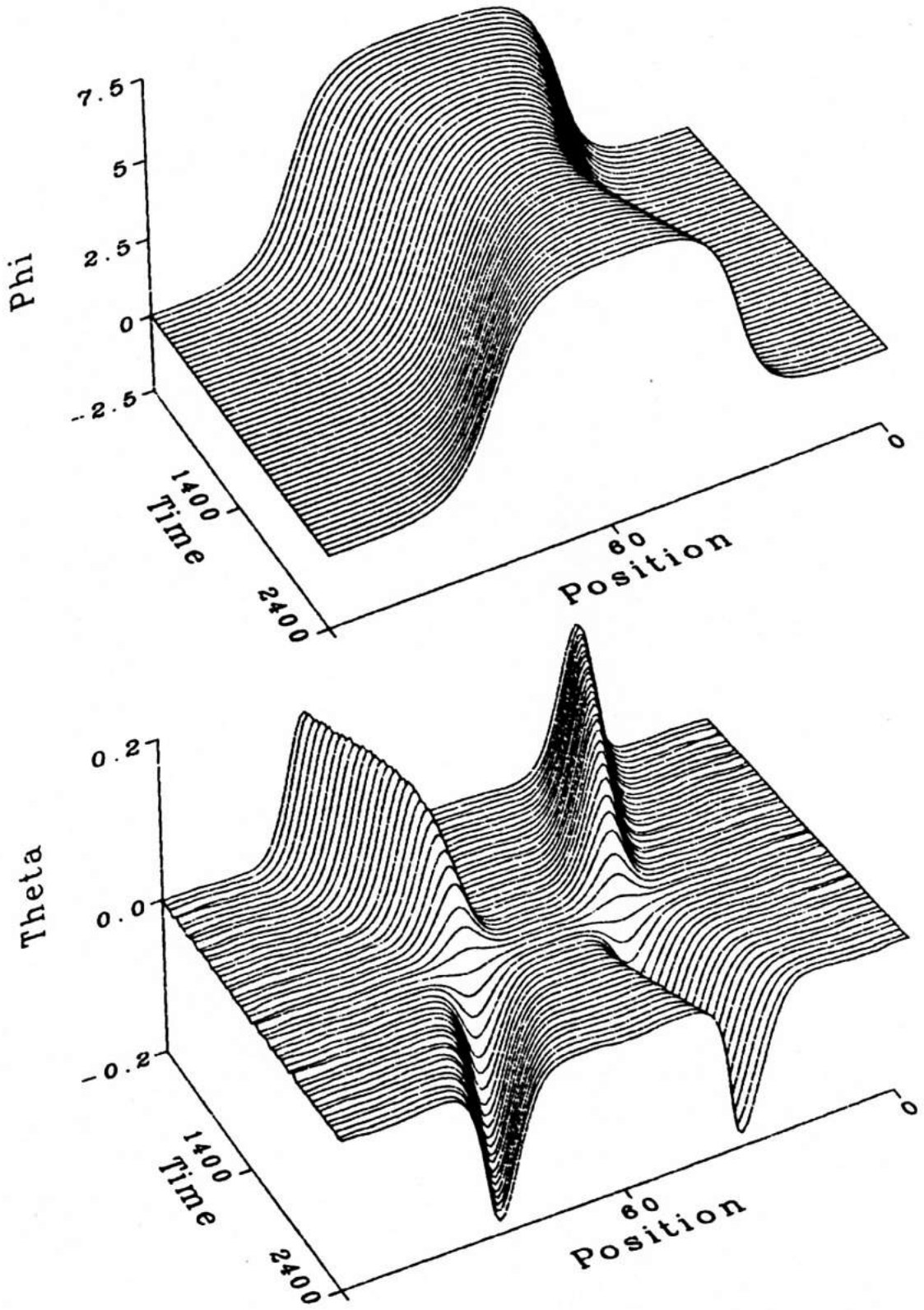

Figure 3.15 Space-time $K\bar{K}$ profile obtained by using a time-averaged initial profile with b = 0.4717, $u_{sG_-} = -0.10$, resulting in a region IV collision. The initial branch III $K\bar{K}$ pair reflects, but the pair remains on branch III. Very little distortion of the initial profile can be detected.

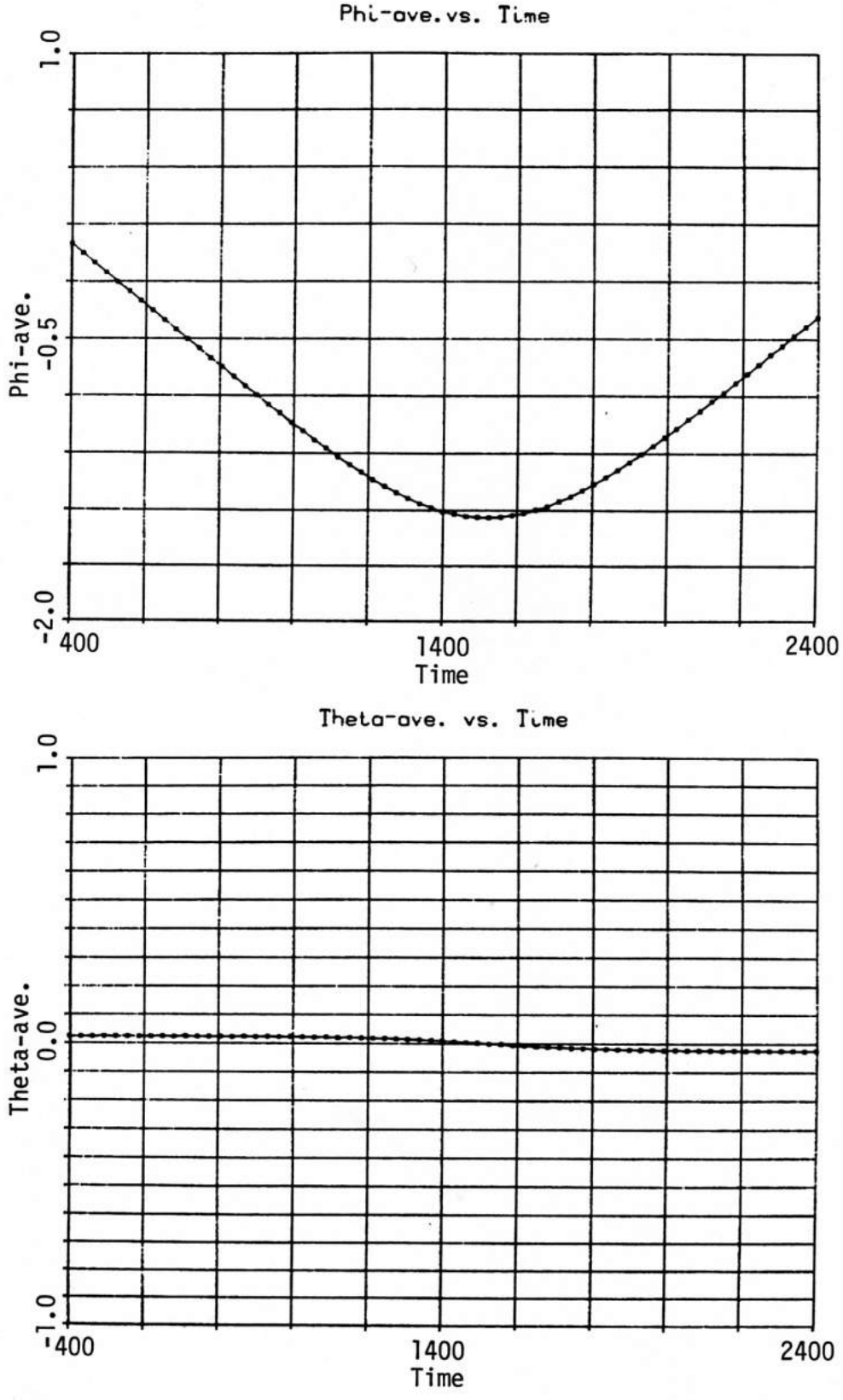

Figure 3.16a Spatial averages of ϕ and θ vs. time for the region IV collision of Figure 3.15.

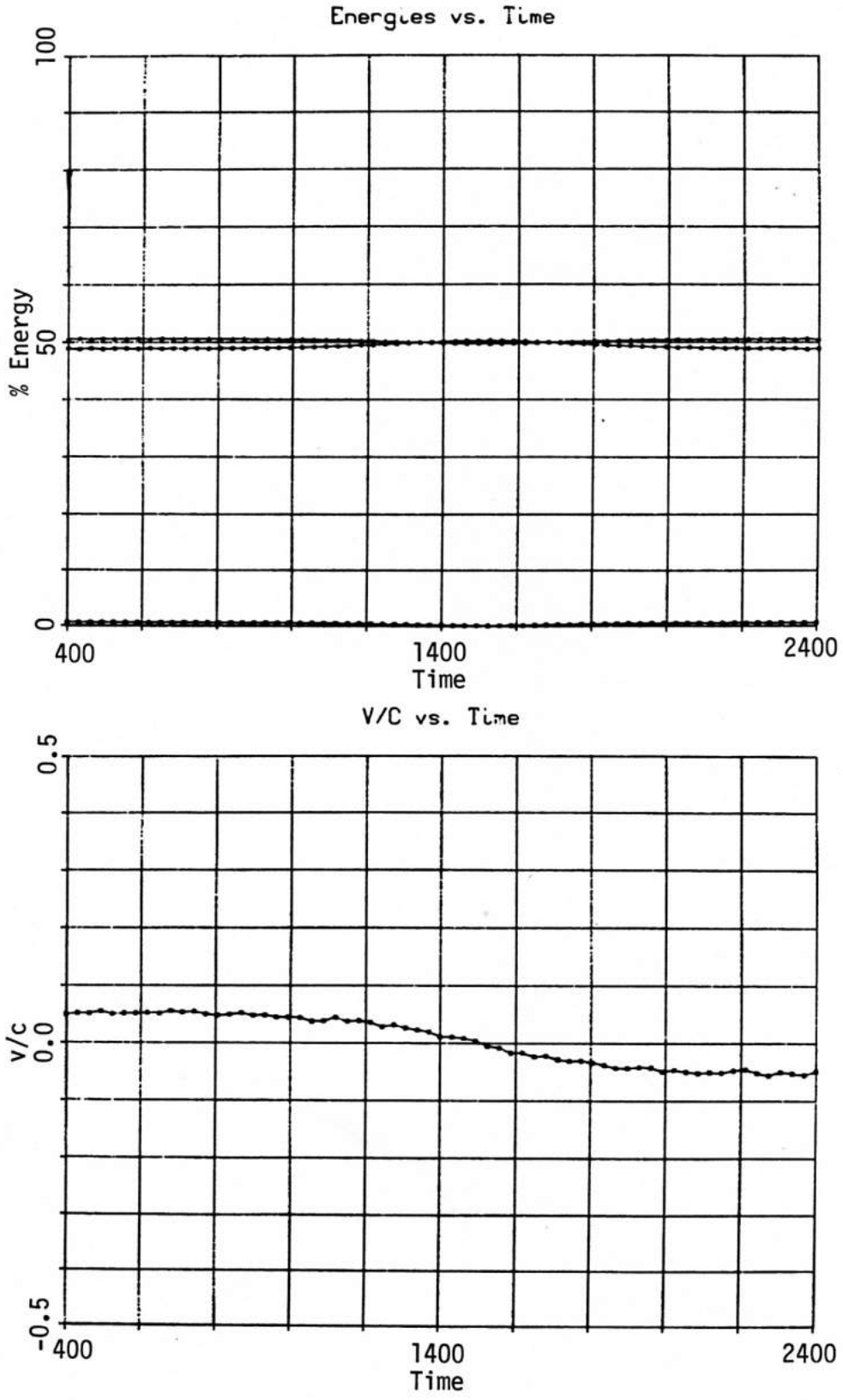

Figure 3.16b Anisotropy (□), field (0), exchange (Δ) energies and velocity vs. time for the region IV collision of Figure 3.15.

oscillatory modes of the kinks are probably responsible for this unusual behavior, in particular, for the breather formation regime and its transmission window.

For the quasi-one-dimensional easy-plane ferromagnet CHAB, the physical parameters are g = 2.0, J = 110 K and A = 5.5 K (Kopinga et al. 1984), so that $\alpha = 2A/J = 0.10$. This is close to the value of α in our numerical work (0.0954), and so the present phase diagram should be directly applicable. (We did these simulations before knowing that experimental data from specific heat measurements on CHAB was available). For easily accessible fields of 5 kG and 30 kG, the parameter b is 0.12 and 0.73 respectively. These are generally in regions II and IV of the phase diagram, leading to breathers or branch III kink reflection. Similarly, for $CsNiF_3$, the physical parameters are g = 2.4, J = 23.6 K and A = 4.5 K (Steiner 1981, Steiner et al. 1983), so that $\alpha = 0.382$. Note that if discreteness effects are unimportant, then the dynamics is determined only by the parameter $b = \beta/\alpha$, and our present phase diagram will suffice. For applied fields B = 5 kG(b = 0.09) and B = 30 kG(b = 0.54), again the final states are generally in the breather formation regime (region II) or the branch III reflection regime (region IV). We have preformed a limited number of simulations with $\alpha = 0.382$ at B = 5 kG and 30 kG to verify this, showing that the discreteness effects were unimportant. Such behavior, however, raises a fundamental issue. Namely, in analyses of statistical properties of $CsNiF_3$ and CHAB (thermodynamics and neutron scattering), the kinks have been assumed to be nearly independent quasiparticles, under sG theory. This assumption is justified on the basis of kink integrity during collisions. But if $K\bar{K}$ scattering leads to generalized breathers, then the fundamental excitations become these breathers, and statistical theories should take this into account. Clearly, the effect of damping on

breather and kink lifetimes needs to be considered, as well as the relative probabilities of thermal nucleation of $K\bar{K}$ pairs versus breathers. Also, most of the neutron scattering attributed to kinks may equally well be due to breather-like states instead. However, if quantum effects are indeed important for these materials, then it is possible that quantum restrictions on out-of-plane motions could make a normalized sG theory fortuitously appropriate.

It is obvious from these results that the sG limit of the equations of motion has severely restricted range of applicability. The sG limit is an important simple model which is easily analyzed, and gives the general kink features within its range of applicability, but does not have the same rich structure as the original easy-plane ferromagnetic Hamiltonian. Although Hamiltonain (2-1) is not known to be integrable, the continuum isotropic limit $A \to 0$ is integrable (Taktajan 1977, Bishop 1980, 1981). Then the principle excitations are breather-like modes which correspond to pulses in the angle of declination with respect to the magnetic field axis. Therefore we expect that in the limit $b \to \infty$ (together with appropriate rescaling of the space and time units, since they depend on A), the branch III kinks become the exact soliton solutions of the isotropic model. Conversely, perhaps a perturbation analysis of the isotropic soliton will be able to produce the approximate profile for the large field limit of the anisotropic model. The large b branch III kinks clearly must be related to the exact pulse modes. Osano (1984) has had similar ideas.

Finally, some comments on the extra bound state (in addition to the zero freqency translation mode), or internal kink mode, for this model. We make a comparison between the present case (applied magnetic field) and

the same Hamiltonian but instead with Ising symmetry breaking[1] (Sklyanin 1979, Mikeska 1981) in the continuum limit. For Ising symmetry breaking an easy axis replaces the unidirectional magnetic field. Then there are no internal kink modes and therefore resonance scattering windows do not exist. Also, the Ising case is known to be completely integrable (Sklyanin 1979), and it appears that complete integrability and bound states are mutually exclusive here as in all known true soliton bearing systems. Thus we emphasize again that the extra bound state in this easy-plane ferromagnet is probably responsible for some of the unusual results we see, both in the single kink dispersion relationships and in $K\bar{K}$ scattering.

There are further studies one can do for this model. In particular, it is experimentally feasible to apply AC driving fields to a sample, and measure the response in a physical property such as the magnetic susceptibility. In the next chapter we numerically investigate the response to combined DC and AC applied fields in various configurations, with phenomenological damping included in the equations of motion. With a DC field in the easy plane, and an AC field along the anisotropy axis, the equations of motion can be reduced (in the $\theta \ll 1$ limit) to the damped driven sine-Gordon equation, which is known to have interesting chaotic dynamics. This and other cases where the dynamics becomes chaotic will be considered next.

---

[1]Note that in Chapters 5 and 6 a similar study of Hamiltonian (2-1) with antiferromagnetic exchange will be presented, and that model will be seen to have a close relationship to this Ising symmetry breaking case.